Extended data figures for "Lattice fluctuation induced pseudogap in quasi-one-dimensional Ta_2NiSe_5"

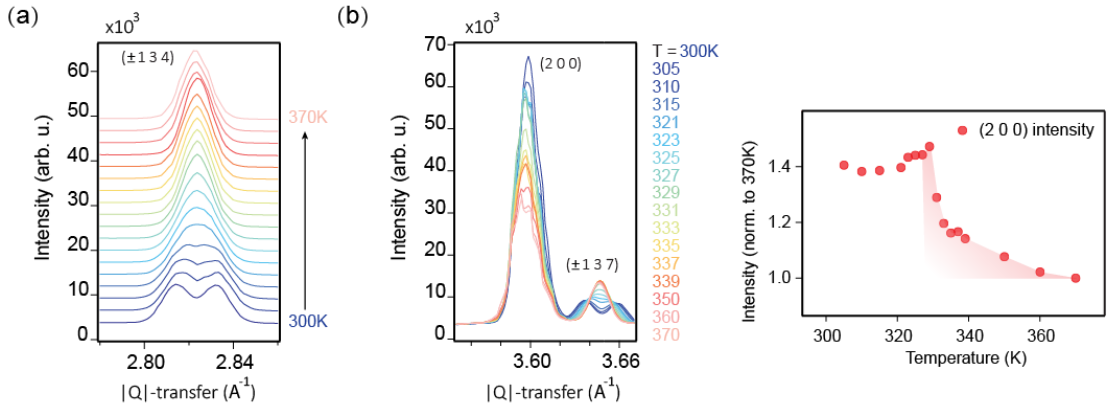

Extended Data Fig. 1| High-energy X-ray scattering data across the structural transition of Ta_2NiSe_5. **(a)** Temperature dependence of the (±1 3 4) peak profile, across the structural transition at T_s~329K. When entering the low temperature monoclinic phase, (1 3 4) and (-1 3 4) peaks are becoming inequivalent and therefore split. **(b)** Temperature dependence of the (2 0 0) Bragg peak and the nearby (±1 3 7) peaks. The peak intensity of (2 0 0) is extracted and plotted on the side, showing response in a broad temperature range above T_s.

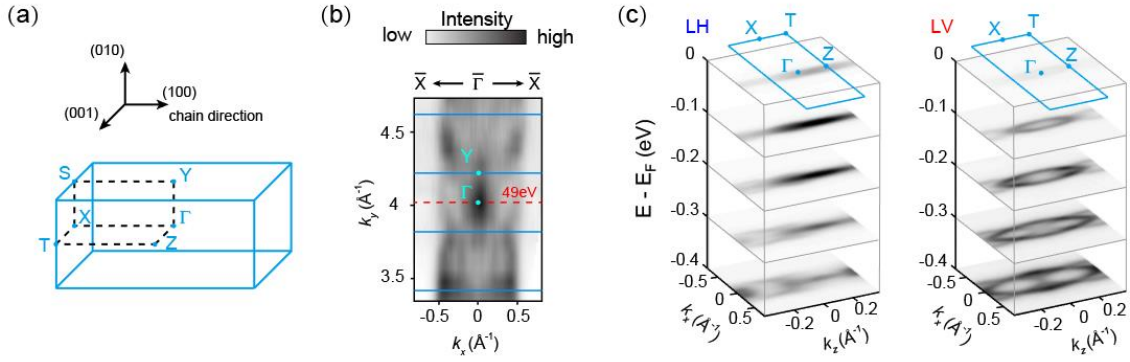

Extended Data Fig. 2| Photoemission data in 3D Brillouin Zone (BZ).

(a) Illustration of BZ of Ta_2NiSe_5 at high-temperature orthorhombic phase. **(b)** Out of plane photoemission map along the k_y direction by changing the photon energy of the incident beam. **(c)** In-plane photoemission map at Γ plane (49eV) with linear horizontal (LH) and linear vertical (LV) polarizations of the incident beam.

The quasi-1D electronic structure of the system is clearly demonstrated. As the shearing of the Ta atoms in the low-temperature monoclinic phase is very small (less than 1%), the BZ can be treated as the same for the whole temperature range.

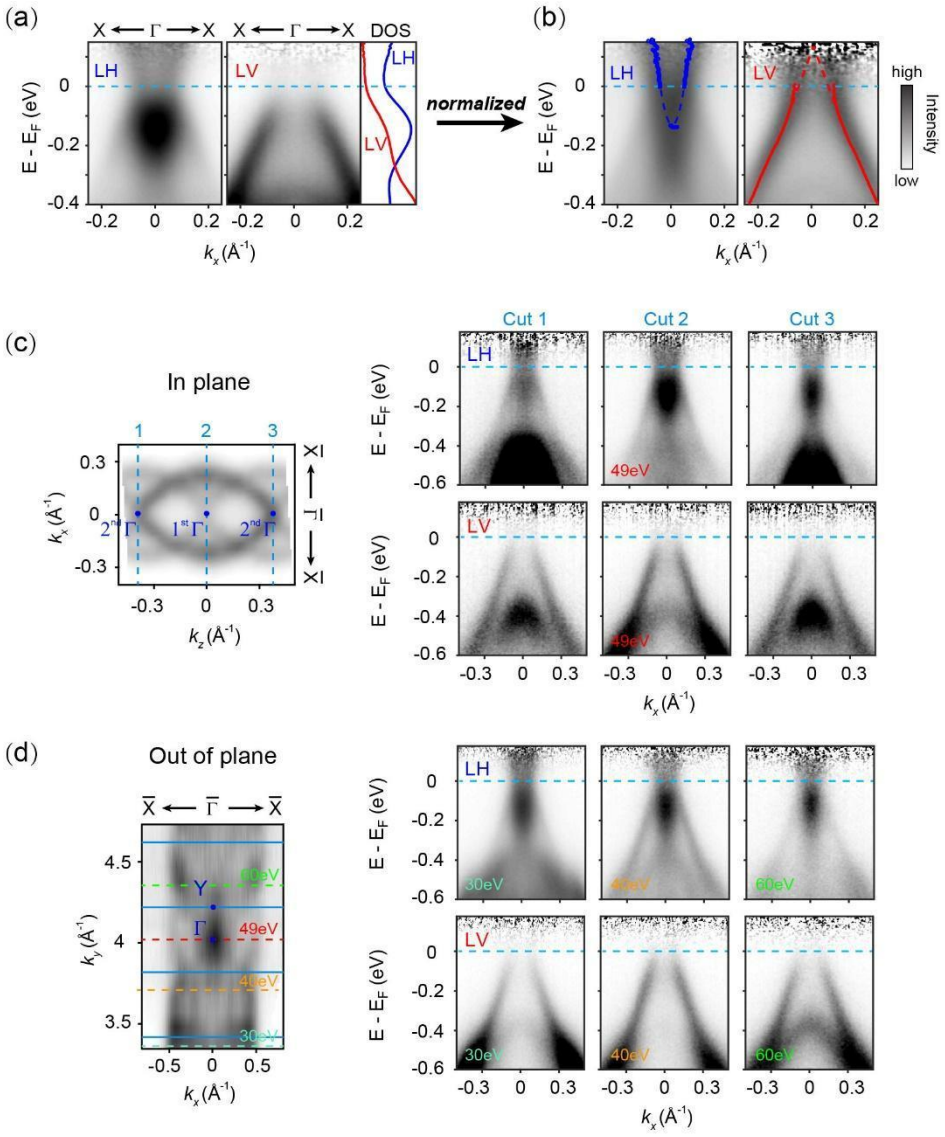

Extended Data Fig. 3| Determination of the pseudogap state at high temperature phase of Ta_2NiSe_5. **(a)** Photoemission spectra of LH and LV polarizations with Fermi Dirac function divided. The integrated density of states (DOS) is plotted on the side, illustrating the spectra weight depletion around Fermi energy (E_F) within both channels. **(b)** Same spectra normalized along energy axes (divided by DOS), to get rid of the effect of spectra weight depletion. Continues dispersions of both conduction and valence bands are recovered with the fitting result overlayed. To further exclude the possibility of matrix element effect, high

symmetry cut $X - \Gamma - X$ at different Brillouin Zones **(c)** and different photon energies of the incident beam (different k_y values) **(d)** were illustrated, where the spectrum weight depletion around E_F is constantly observed.

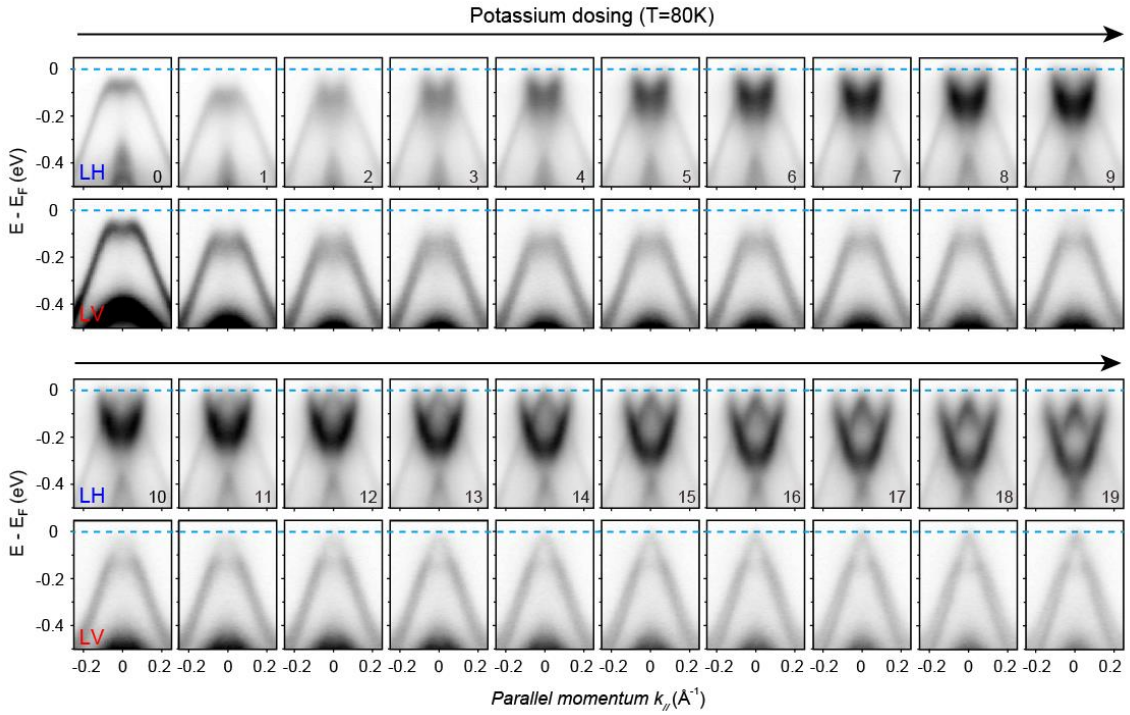

Extended Data Fig. 4| Complete potassium dosing data for both LH and LV polarizations.

The dosing experiment was performed with a photon energy of the incident beam at 84eV (also at the Γ plane in the 3D Brillouin Zone as illustrated in Extended Data Fig. 3), due to the availability of both the polarizations of the light at the beamline. Besides the 3-stages evolution illustrated in LH channel (also Fig. 3 in the main text), the LV channel illustrates the evolution of the valence band with the signal mainly from Ni *3d* orbitals. The tip-like valence band top was gradually recovered, consistent with the DFT calculation for the semi-metallic normal state of the system (main text Fig. 1(c)). A second set of bands can be seen in the background (most distinguishable in 16-19), suggesting the phase separation nature of the system during the transition from the monoclinic phase to the orthorhombic phase. Such behaviour further indicates the structural instability of the system, as a natural result of the presence of fluctuating phonons.

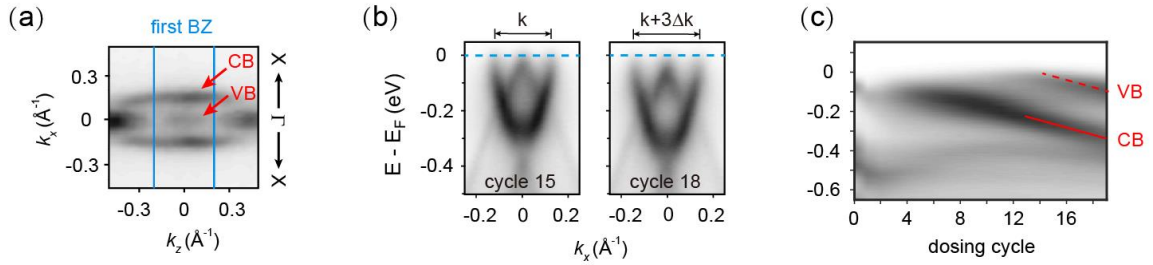

Extended Data Fig. 5| Estimation of electron doping and band shift.

(a) Constant energy contour at Fermi level after potassium dosing, illustrating the quasi-1D nature of the conduction band (CB) and the valence band (VB). Therefore, we only need to consider the $X-\Gamma-X$ direction to estimate the change of the Fermi surface volume in the Luttinger theorem. **(b)** The change of the momentum width along $X-\Gamma-X$ direction is estimated to be ~0.01 Å^{-1} for each dosing cycle, which contributes to a Brillouin Zone portion of roughly 0.01 Å^{-1}/1.79 Å^{-1}=0.56%. Given the existence of two conduction band and one valence band, as well as the spin degeneracy, the total amount of dosage for each cycle is estimated to be roughly 0.56%*6=0.034 electrons per unit cell. **(c)** Evolution of bands at Γ point with dosing cycles.

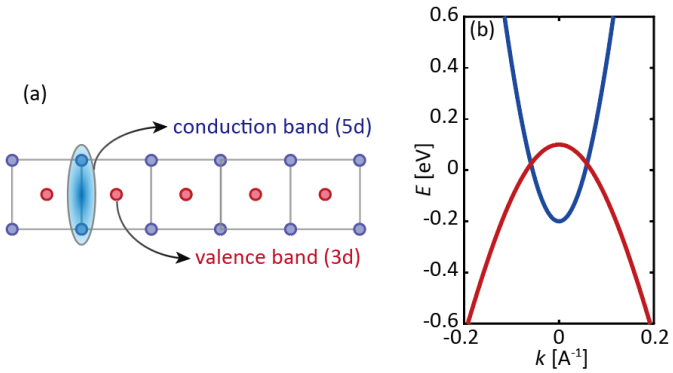

Extended Data Fig. 6| A toy model for the Ta_2NiSe_5 system.

(a) Schematic for the conduction and valence band in the two-band model. **(b)** The non-interacting band structure employed in the simulations uses the fitting result from the experiment (Extended Data Fig. 2 (b)):

$$\varepsilon_k^c = 3.1 - 1.8\,cos\,cos\,k - 0.9\,cos\,cos\,2k - 0.6\,cos\,cos\,3k$$
$$\varepsilon_k^v = -1.8 + 1.5\,cos\,cos\,k + 0.3\,cos\,cos\,2k + 0.1\,cos\,cos\,3k$$

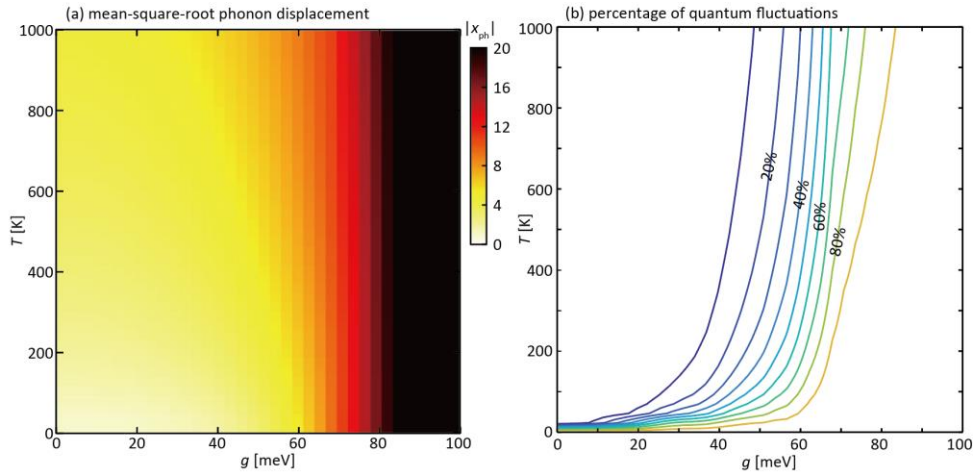

Extended Data Fig. 7| Nature of phonon fluctuation in the system.

Using the exact diagonalization simulation (with twisted averaged boundary conditions), we calculated the average fluctuating displacement represented by the mean-square-root value of phonon displacement operator:

$$|x| = \sqrt{\langle x^2 \rangle} = \sqrt{\langle (a_q + a_{-q}^{\dagger})(a_q + a_{-q}^{\dagger}) \rangle}\Big|_{q=0}$$

(a) The average displacement diverges rapidly with the increase of the e-ph coupling strengths g, which translates to a strong lattice instability and causes the structural transition. The calculation is performed for systems without symmetry breaking, so that the fluctuations are with respect to the orthorhombic phase without any net distortion. **(b)** To quantify the contributions of quantum and thermal fluctuations, the ratio of zero-temperature phonon numbers to the high-temperature ones $\langle n_{ph} \rangle (0) / \langle n_{ph} \rangle (T)$ was evaluated. Assuming the quantum fluctuations, which causes the non-zero phonon numbers at T=0, do not change evidently with temperature, this ratio reflects the relative contributions from quantum origin. We find that the quantum contribution increases rapidly with the coupling strength g and becomes dominant even at room temperature in the strong coupling regime (e.g., the $g = 70meV$ as Fig.4 of the main text).

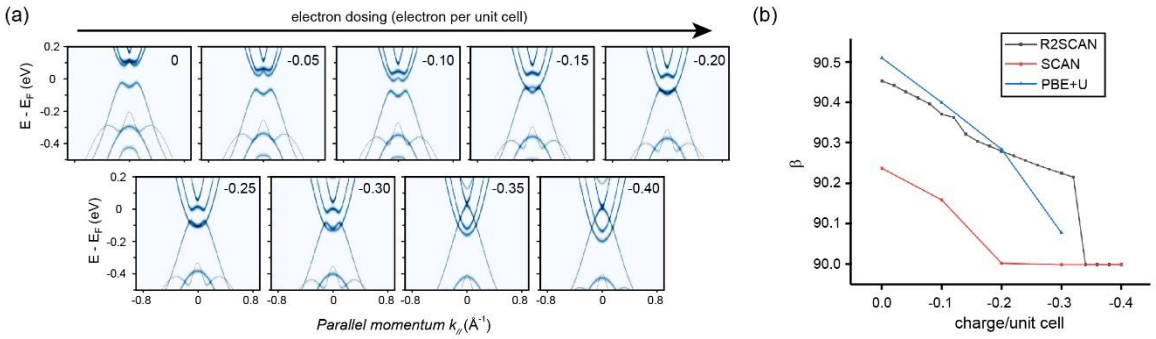

Extended Data Fig. 8| Evolution of band structure with carrier doping by DFT calculation. (a) Evolution of the calculated band structure (r^{2}SCAN function) with carrier doping starting from the low temperature monoclinic fully gapped state. The intensity of Ta 5d orbitals is emphasised. The system shows a natural tendency to recover the high-temperature semi-metallic state with intercepting conduction and valence band upon carrier doping. **(b)** To further confirm such a non-thermal phase transition, the beta angle of the crystal (marking the low-temperature monoclinic structure when deviated from 90 degree) was evaluated with different DFT functionals. Starting from the monoclinic phase, all results suggest the tendency of the system to go back to the orthorhombic phase with additional doping of ~0.3 electron per unit, consistent with the experiment results (main text Fig.3).

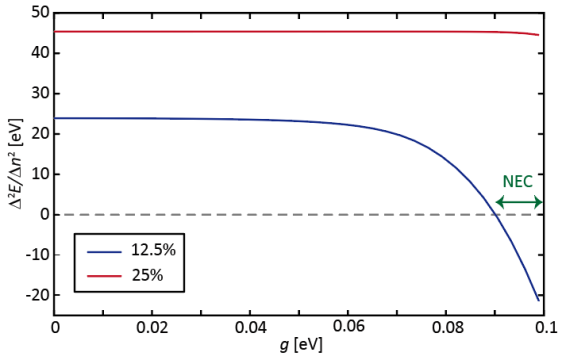

Extended Data Fig. 9| Estimation of electronic compressibility with different dopings and electron-phonon coupling strengths.

Electronic compressibility was estimated through the second derivative of total energy with respect to carrier concentration:

$$\kappa^{-1} \propto \frac{d\mu}{dn} = \frac{d^2E}{dn^2} \approx \frac{E(n+\Delta n) + E(n-\Delta n) - 2E(n)}{\Delta n^2}$$

Due to the finite system size in our simulation, we employ $\Delta n = 0.125$ (Blue line for 12.5% and red line for 25%). With such a large spacing between neighbouring doping levels, the estimated value can be regarded as an average of κ^{-1} within a doping interval. Here, the result comes from the p-type doping, since the effective mass of the electron pocket is smaller, and the narrow NEC regime is averaged within the discrete doping regime.

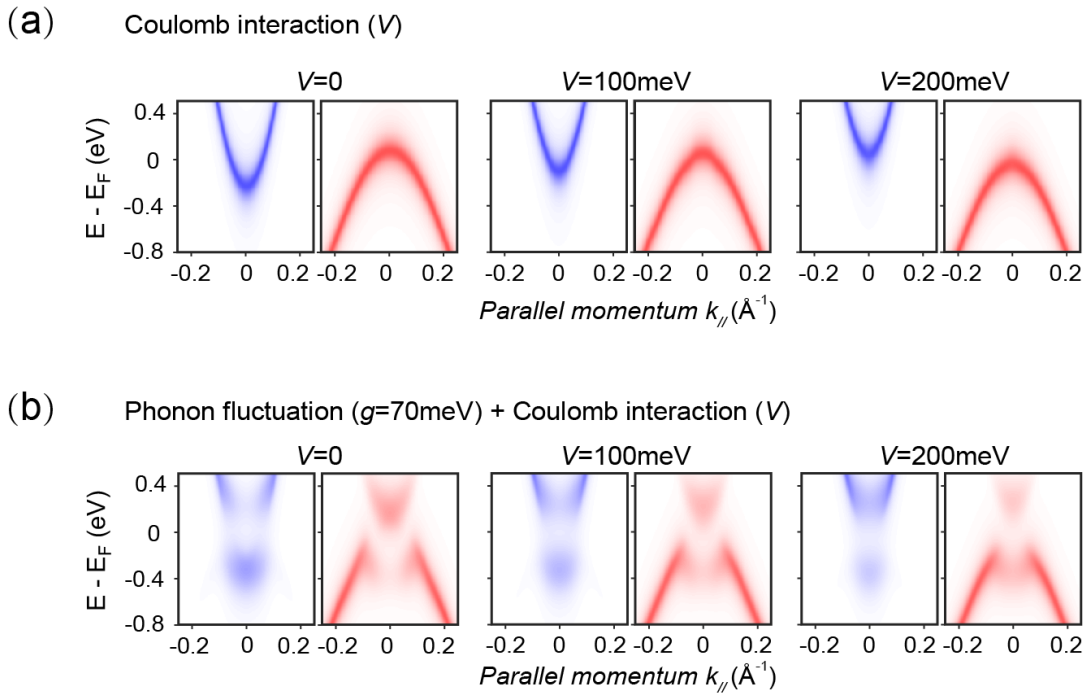

Extended Data Fig. 10| Role of electron-phonon(e-ph) coupling and the direct Coulomb interaction in the system.

To investigate the impact of Coulomb interaction, we include finite inter-band interaction V in the model calculation. **(a)** At the orthorhombic phase without any phonon fluctuations, the increasing Coulomb interaction (increasing V) only leads to a relative band shift without mediating exciton formation. This phenomenon is consistent with the conclusion drawn via the symmetry analysis[23]. **(b)** With finite e-ph coupling ($g = 70meV$) and phonon fluctuations, the Coulomb interaction enhances gap opening and spectral depletion. Therefore, the impact of Coulomb interaction cannot be excluded, but should be regarded as a secondary contribution.

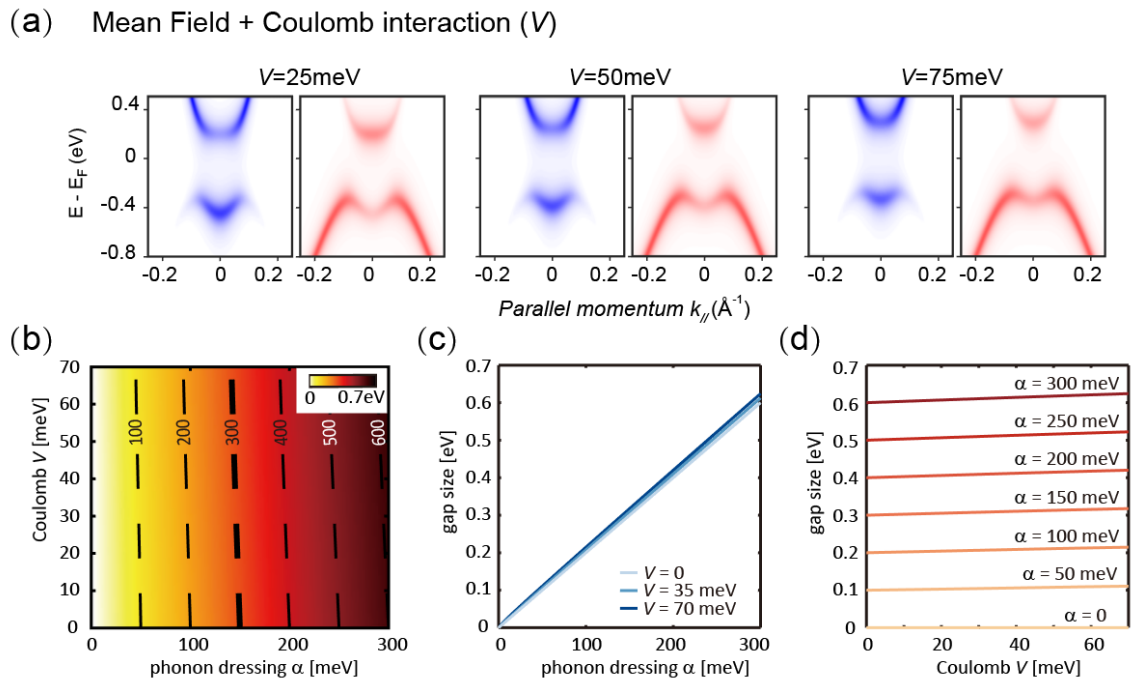

Extended Data Fig. 11| Mean field simulations for system with various strengths of the electron-phonon dressing and Coulomb interaction. The phonon dressing strength is defined $\alpha = g_0 X$, representing the phonon-mediated hopping amplitude between two bands. Here X denotes the lattice displacement as a mean field. **(a)** Simulated band-resolved single-particle spectra for $\alpha = 275$meV (corresponding to $g = 70$meV, same as Fig. 4 of the main text) and additional Coulomb interactions with $V = 25$meV, $V = 50$meV, and $V = 75$meV, respectively. Different from the Extended Data Fig. 10, both the phonon displacement and the Coulomb interaction are treated by the mean-field theory without any fluctuations. **(b)** The mean-field energy gap simulated for various α and V values. The thick line denotes the gap size of Ta_2NiSe_5 estimated by pervious experiments. **(c-d)** the horizontal and vertical cuts of panel (b), representing the dependence on the (mean-field) phonon and Coulomb interaction, respectively.